

Association between oxygen vacancies and trivalent dopants in crystalline and amorphous ZnO

D. Muñoz Ramo,^{1*} A. Chronos,^{1†} M.J.D. Rushton,² and P. D. Bristowe¹

¹*Department of Materials Science and Metallurgy, University of Cambridge,
Cambridge CB2 3QZ, United Kingdom*

²*Department of Materials, Imperial College London, London SW7 2BP, United
Kingdom*

Keywords: ZnO, In:ZnO, amorphous ZnO, DFT, molecular dynamics, Reverse Monte Carlo, defect states, pair distribution function.

Abstract

Density functional theory calculations are used to investigate the structure and binding energies of clusters formed between oxygen vacancies and trivalent dopant atoms (indium, gallium and aluminium) substituted into zinc oxide. Our results show that indium atoms form stable nearest neighbour pairs with oxygen vacancies, while gallium and aluminium atoms associate with them at next nearest neighbour sites. Using a combination of classical molecular dynamics and Reverse Monte Carlo methods, models of amorphous indium zinc oxide at different compositions up to 25 at.% indium are created. Analysis of these models indicates that, in contrast with the trend observed in the crystal phase, indium does not tend to be undercoordinated in the amorphous phase. The value of the band gap obtained for the amorphous compositions is smaller than that of crystalline undoped ZnO by about 0.8 eV and is largely independent of the indium concentration. Electron effective masses calculated in all the amorphous models decrease with increasing amount of indium due to the

* Corresponding author: dm586@cam.ac.uk

† Now at Materials Engineering, The Open University, Milton Keynes MK7 6AA, United Kingdom.

larger dispersion of the In-dominated conduction bands. This trend is compared to resistivity measurements on amorphous indium zinc oxide which also decrease with increasing indium concentration.

1. INTRODUCTION

Transparent conducting oxides (TCOs) such as indium tin oxide (ITO) or indium-doped zinc oxide (IZO) are technologically important in optoelectronic devices.¹⁻⁵ This interest is based on their high electrical conductivity and high optical transmission in the visible region of the e.m. spectrum.³ Recently, IZO has gained in importance compared to ITO because it is relatively less expensive, non-toxic and abundant.⁶⁻⁸

There are numerous density functional theory (DFT) studies on the defect properties of ZnO and IZO.⁸⁻¹⁶ Most of these investigations are concerned with understanding the behaviour of native point defects in these materials. These defects are important for controlling and engineering the conductivity, the dopant distribution, the minority carrier lifetime, the luminescence efficiency, and the degradation of the device.^{17,18} Interestingly, there is a significant spread in the calculated formation energies of point defects in ZnO mainly due to the use of the local density and generalized gradient approximations (LDA and GGA) which poorly describe transition metal oxides.¹⁹

ZnO can be doped *n*-type with trivalent species such as In, Ga or Al and these favourably modify its electrical and optical properties for transparent high-power electronic devices.²⁰⁻²² In the present study we investigate the binding of *n*-type dopants with oxygen vacancies in crystalline ZnO using DFT. Subsequently and in view of these results the structure of amorphous IZO is investigated using classical

molecular dynamics (MD). Finally, we use the Reverse Monte Carlo (RMC) method to generate representative amorphous models of IZO containing only a relatively small number of atoms suitable for use with DFT techniques, and proceed to study their electronic structure.

2. COMPUTATIONAL METHODOLOGY

2.1. DFT calculations

The total energies of the different crystalline structures are calculated using the plane wave DFT code CASTEP.^{19,23} Exchange and correlation interactions are described using LDA or GGA in combination with ultrasoft pseudopotentials.²⁴ The plane wave basis set is expanded to a cut-off of 400 eV and a 2 x 2 x 2 Monkhorst-Pack²⁵ k-point grid is used with a supercell consisting of 72 atoms. Convergence tests indicate that these parameters are numerically converged to 0.1 eV for neutral defect clusters.¹⁸ The unit cell parameters and atomic coordinates are allowed to relax under constant pressure conditions using a Broyden-Fletcher-Goldfarb-Shannon (BFGS) minimizer.²⁶ Replacing a single Zn atom with a *n*-type species in the supercell corresponds to a dopant concentration of about 1 at. %.

Unfortunately, DFT calculations based on LDA or GGA underestimate the band gap of semiconductors leading to erroneous point defect formation energies.²⁷⁻³⁰ For ZnO LDA underestimates the energy of the Zn 3*d* electrons. The Zn *d* states couple with the O *p* states which form the top of the valence band pushing them upwards and effectively reducing the band gap.^{18,31} One way of calculating the under-binding of the Zn *d* electrons is to include of an on-site Coulomb correlation interaction using the so-called LDA+*U* method.^{32,33} LDA+*U* corrects the position of the narrow *d* band states and influences both the valence band maximum (VBM) and

the conduction band minimum (CBM).³⁴ The U correction for Zn $3d$ electrons (labelled U_{3d}) has a strong effect on their energy effectively moving down the $3d$ band, but only has a marginal effect on the band gap.¹⁸ This method is used in the present study *via* a simplified and rotationally invariant approach implemented in CASTEP.^{35,36} The value of U_{3d} which optimizes the position of the $3d$ band is 8.0 eV.

A second way of overcoming the limitations of LDA and GGA is to use hybrid functionals, although their high computational cost restricts them to small systems. In this work, we employ the hybrid B3LYP functional, which has proved to give a good estimate of the ZnO band gap³⁷. This functional is used for the analysis of the electronic structure of the crystalline and amorphous In:ZnO models obtained with the other methods. These calculations have been performed with the CRYSTAL09 code³⁸, which uses a localized basis set to alleviate the computational requirements of the calculations. We re-optimize the atom positions obtained with GGA using the same supercell sizes and k-point mesh as the CASTEP calculations. Oxygen has a basis set consisting of $14s$, $6p$, and $1d$ functions contracted to $1s$, $3sp$, and $1d$ shells using a 8/411/1 scheme. For the cations, we use relativistic effective core potentials (RECP) again to reduce the computational cost. For Zn, we use a Stevens et al. RECP³⁹ that replace all but 10 valence electrons. The related basis set consists of 8 sp and 6 d functions contracted to 3 sp and 2 d shells using a 4211/411 scheme. A Stevens et al. RECP³⁹ is also used for In, with 21 valence electrons and a related basis set of 8 sp and 5 d functions contracted to 4 sp and 3 d shells using a 4121/311 scheme.

2.2. MD calculations

In molecular dynamics Newton's equations of motion are numerically integrated to predict the time evolution of the atomic positions and velocities from a description of the forces acting between them.^{40,41} In this study MD is used to simulate a rapid quench from the molten state (a so-called “melt-quench”), in order to induce an amorphous state. All the simulations are performed using DL_POLY and employ a time-step of 0.4 fs.⁴² The melt-quench algorithm is as follows:

Melt: 50 ps of molecular dynamics is performed in the isothermal-NVT ensemble initially using a Berendsen thermostat to ensure rapid temperature convergence.⁴³ To allow the correct system density to be established, volume relaxation is allowed by then performing a 50 ps MD run in the isothermal-isobaric (NPT) ensemble using a Nosé-Hoover barostat and thermostat (note that all subsequent MD runs are also performed in the NPT ensemble).⁴⁴⁻⁴⁶ The “melt” stage is performed at a temperature of 5000 K; such a high temperature is used in order to ensure that the structure is adequately randomised on the relatively short time-scales accessible by molecular dynamics and in so doing ensures that any structural bias is not inherited from the crystalline starting configuration.

Quench: In order to produce an amorphous structure the randomised structure is cooled rapidly from 5000 K to 300 K. This is achieved by performing a series of 100 fs NPT dynamics runs where the temperature is reduced by 10 K between runs. Finally, on reaching 300 K, the system is equilibrated for a further 50 ps with data collected over the final 2 ps at 1.2 fs intervals.

The pair potential parameters of McCoy-Grimes-Lee are used for all the MD calculations⁴⁷. These employ the Buckingham⁴⁸ potential form to describe short-range interactions, here using a cut-off of 5.5 Å. The long-range Coulombic forces are calculated using the Ewald sum⁴⁹ implemented using a smooth particle mesh

method⁵⁰. The polarisability of In and O atoms is modelled using Dick and Overhauser's shell model.⁵¹ Conventionally, this couples a massless shell to a central core by a harmonic spring with charge shared between the core and shell to give the overall charge of the ion. Here, in a slight modification to the McCoy-Grimes-Lee potentials, shells are assigned a nominal mass of 0.994 amu. In order for the overall mass of each core-shell pair to have the same atomic mass of the species that it represents, the In and O cores are assigned masses of 113.824 and 15.000 amu respectively.

The starting configurations for each doped composition are obtained in the following manner. A 16 x 16 x 10 ZnO supercell containing 10240 atoms with cell parameters of $a = 52.05 \text{ \AA}$, $b = 52.05 \text{ \AA}$ and $c = 52.13 \text{ \AA}$ is constructed. In order to obtain the desired In concentrations (1, 5, 10 and 25 at.%), Zn atoms are randomly substituted for In ions in the perfect ZnO supercell. Charge neutrality is maintained by removing an additional Zn atom for every two In substitutions.

2.3. Reverse Monte-Carlo

Reverse Monte-Carlo is a stochastic optimisation technique, based on the original Metropolis Monte-Carlo method,⁵² which is used to generate configurations consistent with a set of structural data and physical constraints. A detailed description of the RMC algorithm, and its successful application to liquid, disordered and amorphous systems, can be found in previous studies.⁵³⁻⁵⁵ In outline, the RMC algorithm proceeds as follows: a sequence of random atom moves are performed on an atomic configuration of the required composition and density. Each move is accepted or rejected based on whether it improves the fit between the model's

structure factors or pair distribution functions and those of a target system which can be obtained from diffraction experiments or, as here, MD simulations.

Before performing RMC, cubic sub-cells are extracted for each indium composition from the large amorphous MD cells resulting from the MD melt-quench process. These cubes are extracted from the centre of the MD cells and have a number of atoms between 50 and 120 depending on the target composition desired. These sub-cells do not have the exact composition of their parent MD cells, therefore atoms are added and removed at random positions in order to match the In/Zn/O proportions to those of the MD cells. The sub-cells resulting from this process contain several structural artefacts; the periodic boundaries introduced with the sub-cell are not chosen to preserve the local amorphous structure at the cell faces. Likewise the random addition/removal of atoms from the cell is performed without any structural consideration. Here, RMC is used to remove these structural artefacts and in so doing, the aim is to generate configurations that are structurally consistent with the 10240 atom MD cells. In order to further refine the resulting structures, we perform geometry optimization on them with the classical potentials described previously using the Gulp package.⁵⁶

3. RESULTS AND DISCUSSION

3.1. DV_O pairs in crystalline ZnO

Fig. 1 shows the dopant-vacancy(DV_O) pair configurations considered, and Table 1 gives the binding energies of these defect pairs obtained using three exchange-correlation functionals. The distance between the dopant and the oxygen vacancy ranges from first nearest neighbors to third nearest neighbors. Binding energies are a way of examining cluster formation by quantifying the attraction (or

repulsion) between the dopants and the oxygen vacancy. The binding energy of a substitutional D atom to a V_O to form a DV_O pair in ZnO is:

$$E_b(DV_O) = E(DV_O) - E(D) - E(V_O) + E(\text{ZnO}) \quad (1)$$

where $E(DV_O)$, $E(D)$ and $E(V_O)$ are the energies of the supercells containing the defect pair, the substitutional dopant and the oxygen vacancy respectively; $E(\text{ZnO})$ is the energy of the perfect ZnO supercell. In this definition a negative binding energy implies that the defect cluster is more energetically favourable compared to its constituent point defect components.

It is clear from Table 1 that the trends are the same irrespective of the functional used (i.e. GGA, LDA or LDA+ U_{3d}). The $\text{In}V_O$ pair is bound (-0.35 to -0.50 eV) in the nearest neighbor configuration A [Fig. 1(a)], whereas the $\text{Ga}V_O$ and $\text{Al}V_O$ pairs are only bound at the second and third nearest neighbor configurations B and C [Fig. 1(b) and (c) respectively]. The binding energies at these separations, however, are small and therefore the thermal stability of the $\text{Ga}V_O$ and $\text{Al}V_O$ pairs will in turn be limited. Since all the dopant atoms considered here have the same valency (and similar electronegativities) the differences in the binding energies stem mainly from their size differences. In that respect In is the largest dopant considered and the only one that is larger than Zn. Therefore, in the presence of the vacancy the In atom reduces the local strain, whereas for the nearest neighbor $\text{Al}V_O$ and $\text{Ga}V_O$ pairs there is no such advantage. Figure 2 shows the B3LYP density of states (DOS) of the $\text{In}V_O$ configuration A, compared with that of ZnO with only a vacancy. The band gap is mostly unaffected by the presence of In in the lattice. Both in the ZnO and In:ZnO cases a deep localized level is induced, but the presence of In reduces the splitting from the VBM by about 0.4 eV. In what follows we model amorphous IZO and investigate whether there is preferential ordering of oxygen atoms around the In atoms.

That is, does the binding of In atoms with oxygen vacancies in crystalline ZnO imply that In atoms are surrounded by fewer oxygen atoms than Zn atoms in amorphous IZO?

3.2. Modelling amorphous IZO

Figure 3 shows the partial pair distribution functions $g(r)$ for the large (10240 atoms) melt-quenched MD cell (black lines) of a-IZO with 25 at.% In. Similar distributions are found for the 1, 5 and 10 at% In systems. Analysis of the results indicates that there are no systematic changes in the coordination of the O atoms around the In atoms for all the In concentrations considered. However, our DFT calculations on doped crystalline ZnO described in the previous section showed that In would be undercoordinated in the presence of an O vacancy, with a $\text{In}V_{\text{O}}$ binding energy of -0.35 eV to -0.50 eV depending upon the exchange-correlation functional used. The different trend observed in the amorphous models may be due to the way in which these cells are obtained: the initial stages of the classical MD simulations are performed at high temperatures where such binding energies do not affect the evolution of the structure. The subsequent quenching procedure, which is applied over the course of about 5 ps, may be fast enough to conserve these high-energy configurations in the 300 K structures. Figure 3 also shows $g(r)$ for the IZO 120 atom cell (red line) which has been optimized using the RMC method. It is seen that there is good agreement between the RMC and MD pair distribution functions. Similar levels of agreement are obtained for the other In compositions. Tests indicate that the method performs well for smaller cell sizes with lattice parameters down to 8 Å, corresponding to about 50-55 atoms in the cell. Fig. 4 shows as an example the atomic structure of the 120 atom cell for a-IZO with 25 at% In.

3.3. Electronic structure of amorphous IZO

The electronic structure of the supercells obtained through the combined techniques described in section 2 are determined using the hybrid B3LYP functional. Geometry optimization of the atomic positions results in small displacements of the atoms in the cell, of the order of 0.05 Å, which is an indication of the quality of the RMC structures. Figure 5 shows the total and partial DOS for a-IZO containing 10 at. % In and the total DOS for several of the compositions considered. The nature of the valence band near the gap is similar to that of ZnO, with O *p* states predominant. The lower conduction band is composed of a mixture of Zn and In *s* orbitals. The value of one-electron band gap is about 2.5-2.7 eV, with no clear dependence on the amount of In in the lattice. A series of localized occupied levels, induced by undercoordinated O atoms in the structure, are located near the VBM. However, no localized levels are formed in the vicinity of the conduction band minimum; the *s* character of the metal orbitals comprising the CBM allow good overlap between them even in a disordered structure, preventing the formation of dangling bonds and the appearance of localized levels. Electron effective masses m^* are calculated for each composition from the second derivative of the band energies with respect to k in the x, y, and z directions at the Γ -point. For these calculations, six additional a-IZO models are considered with compositions of 22, 29, 32, 33, 34.8 and 35.2 at.% In. The values obtained display little anisotropy as expected for an amorphous system. Figure 6 shows the average effective masses $\langle m^* \rangle$ obtained, along with values calculated for c-ZnO and c-In₂O₃. The results show a clear reduction in $\langle m^* \rangle$ as the In concentration increases until reaching saturation at the concentration of 32 at.% In (equivalent to an In/(In+Zn) atomic ratio of 0.76). The trend is in agreement with experimental resistivity data⁵⁷.

The main driving force for the decrease in electron effective mass is the increasing contribution of the In *s* states at the bottom of the conduction band, which enhances band dispersion. This enhancement is correlated with the changes in structure of the amorphous cell, where an increasing number of InO_x units become linked to each other and provide favoured pathways for the electron conduction.

4. CONCLUSIONS

Several computational techniques are used in combination to investigate the atomic and electronic properties of crystalline ZnO doped with In, Ga, or Al and amorphous IZO. DFT calculations reveal that indium dopants attract first nearest neighbour oxygen vacancies in crystalline ZnO, whereas dopants such as gallium or aluminium do not. With the use of MD it is predicted that there is no preferential ordering of oxygen around indium in amorphous IZO. We introduce a novel and efficient MD-RMC technique to simulate the structure of amorphous IZO alloys using small cells, and find that the band gap of the amorphous phase is smaller than in crystalline phases and largely independent of the indium composition. Finally, we observe a decrease of the electron effective mass with increasing In content due to an increase in band dispersion induced by the In *s* states at the bottom of the conduction band. The trend is consistent with resistivity measurements on a-IZO as a function of In composition.

ACKNOWLEDGEMENTS

Financial support for this work is provided by the European Commission through contract No. NMP3-LA-2010-246334 (ORAMA).

References

- ¹J. M. Phillips, R. J. Cava, G. A. Thomas, S. A. Carter, J. Kwo, and T. Siegrist, Appl. Phys. Lett. **67**, 2246 (1995).
- ²J. A. Zuo and A. Erbe, Phys. Chem. Chem. Phys. **12**, 11467 (2010).
- ³Special Issue of Transparent Conducting Oxides, edited by D. S. Ginley and C. Bright [MRS Bull. **15** (2000)].
- ⁴M. Gabas, S. Gota, J. R. Ramos-Barrado, M. Sánchez, N. T. Barrett, J. Avila, and M. Sacchi, Appl. Phys. Lett. **86**, 042104 (2005).
- ⁵P. Sharma, A. Gupta, K. V. Rao, F. J. Owens, R. Sharma, R. Ahaja, J. M. O. Guillen, B. Johansson, and G. A. Gehring, Nat. Mater. **2**, 673 (2003).
- ⁶J. F. Wager, Science **300**, 1245 (2003).
- ⁷K. Nomura, H. Ohta, K. Veda, T. Kamiya, M. Hirano, and H. Hosono, Science **300**, 1269 (2003).
- ⁸X. H. Zhou, Q. H. Hu, and Y. Fu, J. Appl. Phys. **104**, 063703 (2008).
- ⁹S. B. Zhang, S. H. Wei, and A. Zunger, Phys. Rev. B **63**, 075205 (2001).
- ¹⁰S. Lany and A. Zunger, Phys. Rev. B **72**, 035215 (2005).
- ¹¹C. H. Patterson, Phys. Rev. B **74**, 144432 (2006).
- ¹²A. Janotti and C. G. Van de Walle, Nat. Mater. **6**, 44 (2007).
- ¹³S. Lany and A. Zunger, Phys. Rev. Lett. **98**, 045501 (2007).
- ¹⁴J. M. Carlsson, H. S. Domingos, P. D. Bristowe, and B. Hellsing, Phys. Rev. Lett. **91**, 165506 (2003).
- ¹⁵Z. Lin and P. D. Bristowe, J. Appl. Phys. **106**, 013520 (2009).
- ¹⁶W. Körner and C. Elsässer, Phys. Rev. B **81**, 085324 (2010).
- ¹⁷Deep Centers in Semiconductors: A State-of-the-Art Approach, 2nd ed., edited by S. T. Pantelides (Gordon and Breach Science, Yverdon, 1992).
- ¹⁸A. Janotti and C. G. Van de Walle, Phys. Rev. B **75**, 165202 (2007).
- ¹⁹M. C. Payne, M. P. Teter, D. C. Allan, T. A. Arias, and J. D. Joannopoulos, Rev. Mod. Phys. **64**, 1045 (1992).
- ²⁰K. J. Kim and Y. R. Park, Appl. Phys. Lett. **78**, 475 (2001).

- ²¹J. G. Lu, S. Fujita, T. Kawaharamura, H. Nishinaka, Y. Kamada, T. Ohshima, Z. Z. Ye, Y. J. Zeng, Y. Z. Zhang, L. P. Zhu, H. P. He, and B. H. Zhao, *J. Appl. Phys.* **101**, 083705 (2007).
- ²²Y. L. Wang, F. Ren, W. Lim, D. P. Norton, S. J. Perton, I. I. Krarchenko, and J. M. Zarada, *Appl. Phys. Lett.* **90**, 232103 (2007).
- ²³S. J. Clark, M. D. Segall, C. J. Pickard, P. J. Hasnip, M. J. Probert, K. Refson, and M. C. Payne, *Z. Kristallographic* **220**, 567 (2005).
- ²⁴D. Vanderbilt, *Phys. Rev. B* **41**, 7892 (1990).
- ²⁵H. J. Monkhorst and J. D. Pack, *Phys. Rev. B* **13**, 5188 (1976).
- ²⁶T. H. Fischer and J. Almlof, *J. Phys. Chem.* **96**, 9768 (1992).
- ²⁷E. R. Batista, J. Heyd, R. G. Hennig, B. P. Uberuaga, R. L. Martin, G. E. Scuseria, C. J. Umrigar, and J. W. Wilkins, *Phys. Rev. B* **74**, 121102 (2006).
- ²⁸H. Bracht and A. Chroneos, *J. Appl. Phys.* **104**, 076108 (2008).
- ²⁹S. Lany and A. Zunger, *Phys. Rev. B* **78**, 235104 (2008).
- ³⁰P. Rinke, A. Janotti, M. Scheffler, and C. G. Van de Walle, *Phys. Rev. Lett.* **102**, 026402 (2009).
- ³¹S. H. Wei and A. Zunger, *Phys. Rev. B* **37**, 8958 (1988).
- ³²V. I. Anisimov, I. V. Solovyev, M. A. Korotin, M. T. Czyzyk, and G. A. Sawatzky, *Phys. Rev. B* **48**, 16929 (1993).
- ³³A. I. Liechtenstein, V. I. Anisimov, and J. Zaanen, *Phys. Rev. B* **52**, R5467 (1995).
- ³⁴A. Janotti, D. Segev, and C. G. Van de Walle, *Phys. Rev. B* **74**, 045202 (2006).
- ³⁵S. L. Dudarev, G. A. Botton, S. Y. Savrasov, C. J. Humphreys, and A. P. Sutton, *Phys. Rev. B* **57**, 1505 (1998).
- ³⁶M. Cococcioni and S. de Gironcoli, *Phys. Rev. B* **71**, 035105 (2005).
- ³⁷C. H. Patterson, *Phys. Rev. B* **74**, 144432 (2006).
- ³⁸R. Dovesi, V. R. Saunders, C. Roetti, R. Orlando, C. M. Zicovich-Wilson, F. Pascale, B. Civalleri, K. Doll, N. M. Harrison, I. J. Bush, P. D'Arco, and M. Llunell, *CRYSTAL09 User's Manual* (University of Torino, Torino, 2009).
- ³⁹W. J. Stevens, M. Krauss, H. Basch, and P. G. Jasien, *Can. J. Chem.* **70**, 612 (1992).

- ⁴⁰M. P. Allen and D. J. Tildesley, *Computer Simulation of Liquids*, Oxford University Press, 1989.
- ⁴¹D. C. Rapaport, *The Art of Molecular Dynamics Simulation*, Cambridge University Press, 2004.
- ⁴²W. Smith and I. T. Todorov, *Molecular Simulation* **32**, 935 (2006).
- ⁴³H. J. C. Berendsen, J. P. M. Postma, W. G. Van Gunsteren, A. DiNola, and J. R. Haak, *J. Chem. Phys.* **81**, 3684 (1984).
- ⁴⁴S. Nosé, *Molecular Phys.* **52**, 255 (1984).
- ⁴⁵S. Nosé, *J. Chem. Phys.* **81**, 511 (1984).
- ⁴⁶W. Hoover, *Phys. Rev. A* **31**, 1695 (1985).
- ⁴⁷M. A. McCoy, R. W. Grimes, and W. E. Lee, *Philos. Mag. A* **76**, 1187 (1997).
- ⁴⁸R. A. Buckingham, *Proc. Royal Soc. London Series A, Math. Phys. Sci.* **168**, 264 (1938).
- ⁴⁹P. P. Ewald, *Ann. Phys.* **64**, 253 (1921).
- ⁵⁰U. Essmann, L. Perera, M. L. Berkowitz, T. Darden, H. Lee, and L. G. Pedersen, *J. Chem. Phys.* **103**, 8577 (1995).
- ⁵¹B. Dick and A. Overhauser, *Phys. Rev.* **112**, 90 (1958).
- ⁵²N. Metropolis, A. W. Rosenbluth, M. N. Rosenbluth, A. H. Teller, and E. Teller, *J. Chem. Phys.* **21**, 1087 (1953).
- ⁵³R. L. McGreevy and L. Pusztai, *Molecular Simulation* **1**, 359 (1988).
- ⁵⁴D. A. Keen and R. L. McGreevy, *Nature* **344**, 423 (1990).
- ⁵⁵O. Gereben, P. Jovari, L. Temleitner, L. Pusztai, *J. Optoelectron. Adv. Mater.* **9**, 3021 (2007).
- ⁵⁶J. Gale and A. L. Rohl, *Mol. Simul.* **29**, 291 (2003).
- ⁵⁷E. Fortunado, P. Barquinho, and R. Martins, *Adv. Mat.* **24**, 2945 (2012).

TABLE 1. Binding energies (eV) of the neutral InV_O , GaV_O and AlV_O defect pairs for the A, B and C configurations shown in Fig. 1 using the GGA, LDA and LDA+ U_{3d} exchange-correlation functionals.

GGA			
Defect pair	A	B	C
InV_O	-0.39	0.01	-0.01
GaV_O	0.49	-0.06	-0.07
AlV_O	1.05	-0.08	-0.07
LDA (LDA+ U_{3d})			
Defect pair	A	B	C
InV_O	-0.50 (-0.35)	0	-0.03
GaV_O	0.33 (0.52)	-0.13	-0.12
AlV_O	1.13 (1.33)	-0.18	-0.16

CAPTIONS FOR FIGURES

Fig. 1 (color online): Schematic representation of (a) the nearest neighbour DV_O pair (configuration A), (b) the 2nd nearest neighbour DV_O pair (configuration B) and (c) the 3rd nearest neighbour DV_O pair (configuration C). Red and green spheres represent the O and Zn atoms respectively; D (In, Ga or Al) is represented by a purple sphere and the O vacancy by a black sphere.

Fig. 2 (color online): B3LYP DOS of (a) c-ZnO with an O vacancy, and (b) c-In:ZnO with an O vacancy in the nearest neighbour position (configuration A). Arrow indicates the CBM. Peaks between 0.4-0.8 eV above the VBM are localized defect states.

Fig. 3 (color online): Comparison between partial pair distribution functions for the large MD cell (black line) and the 120 atom cell (red line) optimized using the Reverse Monte Carlo method for the a-IZO system with 25 at.% In.

Fig. 4 (color online): Atomic structure of the 120 atom a-IZO system containing 25 at.% In following reverse Monte-Carlo optimisation. Red, green and purple spheres represent O, Zn and In atoms respectively.

Fig. 5 (color online): (a) Total and partial DOS of a-IZO containing 10 at.% In. (b) Total DOS of a-IZO for different In doping levels. States localized near the VBM are occupied and due to undercoordinated O atoms. No states deep in the band gap are observed.

Fig. 6: Average electron effective mass $\langle m^* \rangle / m_e$ in a-IZO with respect to In atomic ratio. Circles show values for crystalline ZnO and In_2O_3 .

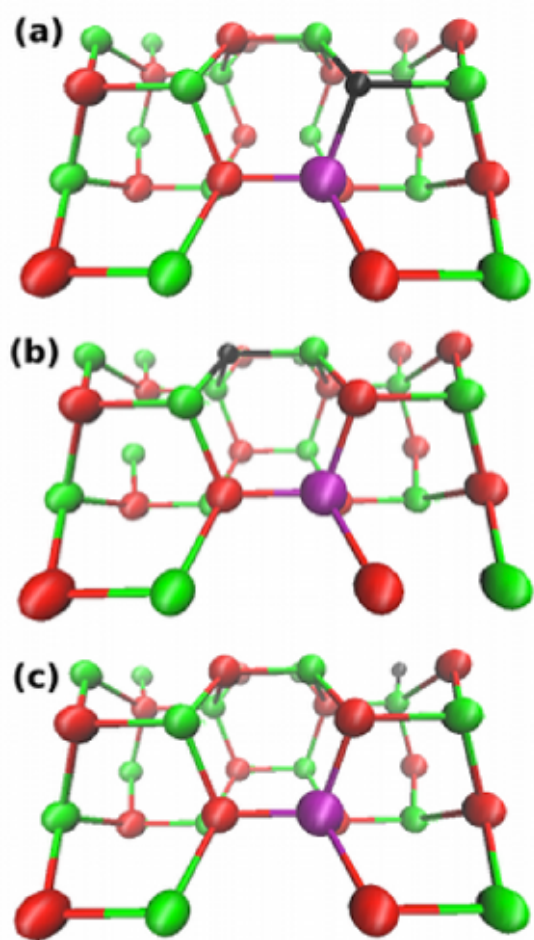


Figure 1

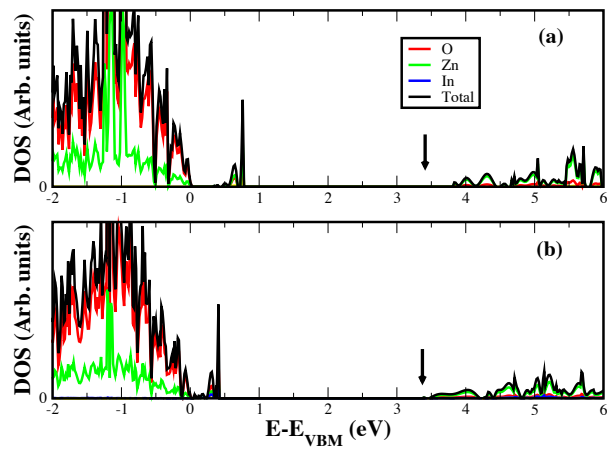


Figure 2

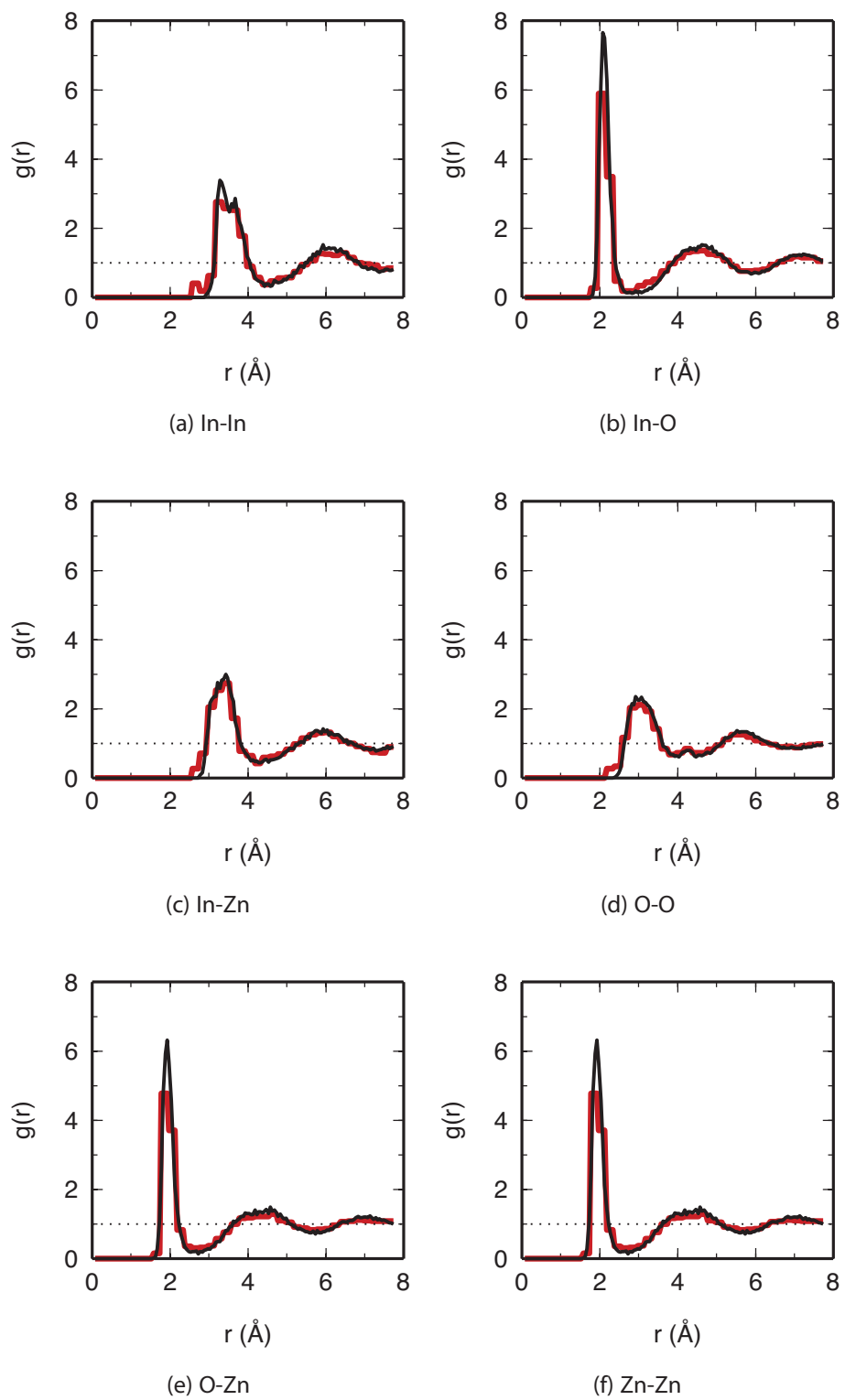


Figure 3

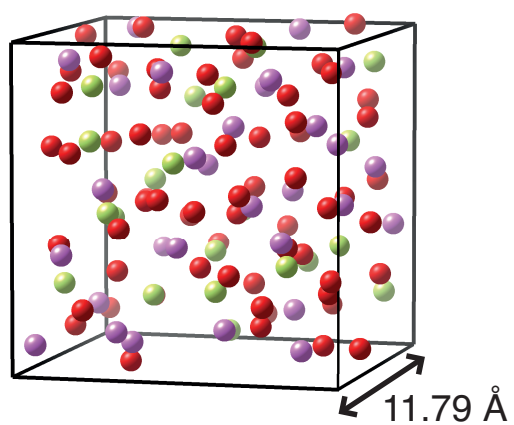


Figure 4

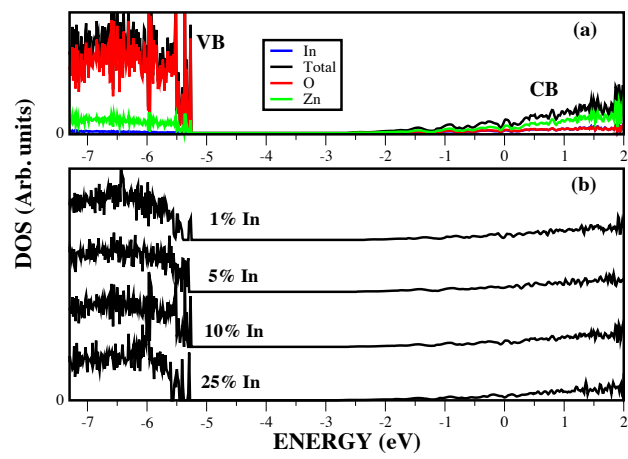


Figure 5

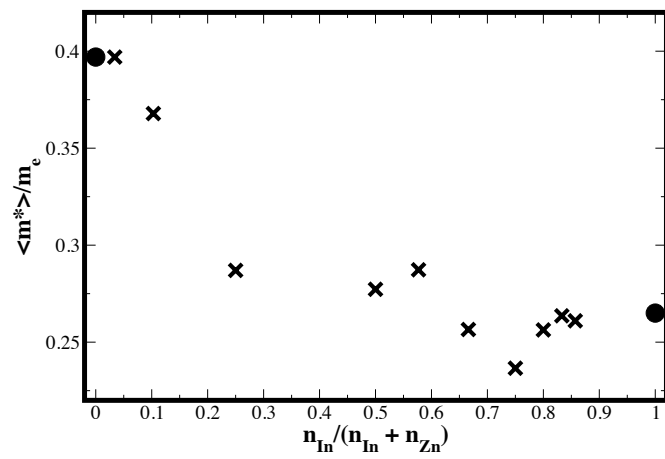


Figure 6